

Simulation of capillary infiltration into packing structures by the Lattice-Boltzmann method for the optimization of ceramic materials

Danilo Sergi,¹ Loris Grossi,¹ Tiziano Leidi,¹ and Alberto Ortona¹

¹*University of Applied Sciences SUPSI, The iCIMS Research Institute, Galleria 2, CH-6928 Manno, Switzerland*

(Dated: July 28, 2016)

In this work we want to simulate with the Lattice-Boltzmann method in 2D the capillary infiltration into porous structures obtained from the packing of particles. The experimental problem motivating our work is the densification of carbon preforms by reactive melt infiltration. The aim is to determine optimization principles for the manufacturing of high-performance ceramics. Simulations are performed for packings with varying structural properties. Our analysis suggests that the observed slow infiltrations can be ascribed to interface dynamics. Pinning represents the primary factor retarding fluid penetration. The mechanism responsible for this phenomenon is analyzed in detail. When surface growth is allowed, it is found that the phenomenon of pinning becomes stronger. Systems trying to reproduce typical experimental conditions are also investigated. It turns out that the standard for accurate simulations is challenging. The primary obstacle to overcome for enhanced accuracy seems to be the over-occurrence of pinning.

Keywords: Lattice-Boltzmann method, Pore-scale simulations for capillary infiltration, Packing structures, Reaction-bonded ceramics

1. INTRODUCTION

Porous media are ubiquitous in science and engineering. Typical examples ripple across a number of disciplines such as hydrology, oil recovery, materials science, printing and solar technology, to cite but a few (Bear, 1972; Dullien, 1992; Furler et al., 2012; Goodall & Mortensen, 2013; Koponen et al., 1998). In simulations, their structures are investigated according to a variety of properties (mechanical, thermal and fluid dynamics) mainly through finite elements methods (FEM) (Alawadhi, 2010; Bohn & Garboczi, 2003). Capillarity is the spontaneous infiltration of a fluid into a porous medium (Alava, Dube, & Rost, 2004; Washburn, 1921). The adhesive forces between the liquid and solid phases are responsible for this phenomenon. Indicatively, its characteristic length scale is the micron (de Gennes, Brochard-Wyart, & Quéré, 2004). Our interest is in the role of the porous structure for capillary infiltration. Simulations are carried out by using the Lattice Boltzmann (LB) method (Benzi, Succi, & Vergassola, 1992; Chen & Doolen, 1998; Succi, 2009; Sukop & Thorne, 2010; Wolf-Gladrow, 2005). This is a numerical scheme for approximating the hydrodynamic behavior, especially suited for problems involving complex boundaries and interface phenomena. Its main advantage over other approaches resides in the discretization of the velocity space and a statistical treatment of particle motion and collisions. Applications encompass disparate critical systems (Bao et al, 2014; Ghosh, Patil, Mishra, Das, & Das, 2012; Haghani, Rahimian, & Taghilou, 2013; Joshi & Sun, 2010; Liu, Valocchi, & Kang, 2012; Wang & Pan, 2008). The accuracy is in general comparable with that of studies in computational fluid dynamics (CFD) based on FEM (Succi, 2009).

The actual problem motivating our research is the reactive infiltration of molten silicon (Si) into carbon (C) preforms (Bougiouri, Voytovych, Rojo-Calderon, Narciso, & Eustathopoulos, 2006; Dezellus & Eustathopoulos, 2010; Dezellus, Hodaj, & Eustathopoulos, 2003; Einset, 1996, 1998; Eustathopoulos, 2015; Eustathopoulos, Nicholas, & Drevet,

1999; Hillig, Mehan, Morelock, DeCarlo, & Laskow, 1975; Israel et al., 2010; Liu, Muolo, Valenza, & Passerone, 2010; Messner & Chiang, 1990; Mortensen, Drevet, & Eustathopoulos, 1997; Voytovych, Bougiouri, Calderon, Narciso, & Eustathopoulos, 2008). This is a complex phenomenon associated with a wetting transition and surface growth. A feature of this process is that Si reacts with C to form silicon carbide (SiC). Si wets SiC but does not wet C (Bougiouri et al., 2006). Furthermore, the reaction-formed phase causes the thickening of the surface behind the invading front (Bougiouri et al., 2006; Einset, 1996, 1998; Israel et al., 2010; Messner & Chiang, 1990). The interaction with the fluid flow results in a retardation of the infiltration up to its interruption because of pore clogging. This research gains increasing attention also in industrial practice. Liquid Si infiltration (LSI) is a common manufacturing route to high-performance ceramics. Prominent advanced applications include armor and brake systems (Fan et al., 2008; Krenkel & Berndt, 2005; Roberson & Hazell, 2003). Significant engineering efforts concentrate on the control of the effects of reactivity. Indeed, SiC formation provides additional hardness to the resulting ceramic material, reducing also the amount of residual unreacted Si detrimental for high-temperature functioning. On the other hand, pore closure can stop infiltration before full densification is attained. The microstructure of the C preform is of course of importance for optimal impregnation, besides for the operating behavior of the final ceramic product in specific applications (e.g., the length of reinforced C fibers) (Aghajanian et al., 2013; Gadow, 2000; Gadow & Speicher, 2000; Israel et al., 2010; Paik et al., 2002; Salamone, Karandikar, Marshall, Marchant, & Sennett, 2008).

In previous works we have studied the effects of surface growth for systems composed of single capillaries both uniform and structured in 2D (Sergi, Grossi, Leidi, & Ortona, 2014, 2015). The focus of the present investigation is on making more precise the pore configurations of particular relevance for the industrial application of LSI. The strategy consists in first realizing porous structures approximating real

porous preforms. To this end, we generate packing systems by using particles differing in basic attributes (size, shape and distribution). In principle, these parameters can be controlled by the selection and processing of powders. The packing structures are assembled by means of the random sequential addition (Sherwood, 1997; Widom, 1966). This is a simple and effective algorithm allowing to reach reasonable volume fractions for random packings. The simulations for capillary infiltration aim at highlighting the function of specific pore and structural characteristics. The systems of this work display enhanced randomness with pores and channels of different size and orientation inducing complex dynamics for the invading front. The significance of this investigation resides in the possibility to translate the findings into inputs for preform preparation in order to improve the quality of ceramic materials.

Our simulations indicate that the interface dynamics can be assumed to be responsible for small effective radii. Pinning of the contact line is the primary process affecting capillary infiltration. Our work allows to give evidence for the mechanism determining pinning in random systems. Packings of particles based on bimodal size distributions turn out to provide features reducing the strong retardation of liquid invasion associated with pinning. Larger particles introduce walls creating channels that are filled faster while smaller particles make the pore structure more uniform. As a result, the interface travels longer distances before the loss of its curvature. Furthermore, the probability to encounter the surface of other particles is higher. Our data also show that the inertia effects induced by accelerations remain of secondary importance. With surface growth, it is found that pore closure can be effective and pinning turns out to be enhanced. The retardation effects are stronger for fast infiltrations (higher degree of orientation disorder), that remain nevertheless more advantageous. Also with surface growth, bimodal size distributions lead to better results. Simulations with higher resolution for the porous structure are also performed for a direct comparison with experimental expectations. In this case, the effect of surface growth on pore closure is mainly indirect because pinning is stronger. Furthermore, the relative strength of capillary forces is too weak. This means that the details of the infiltration process suffers from discrepancies with real conditions. For example, this implies that the ratio of the infiltrated distance to the thickness of the growing surface (i.e., the width of the reaction-formed phase) is too small in simulations. Progress seem possible especially by reducing the phenomenon of pinning.

2. MODELS AND ANALYSIS

For the formalism of the LB models the interested reader is addressed to Sergi et al. (2014). In the sequel, the same notation and terminology are employed. We recall that in experiments with molten Si and some alloys the invading front exhibits a kinetics linear with time (Israel et al., 2010; Voytovych et al., 2008). The standard Washburn law for capillary infiltration in vacuum predicts a parabolic time depen-

dence. The observed experimental behavior can be reproduced with the simulations by assuming that the systems are composed by two fluid components (Chibbaro, 2008; Chibbaro, Biferale, Diotallevi, & Succi, 2009; Diotallevi, Biferale, Chibbaro, Lamura, et al., 2009; Diotallevi, Biferale, Chibbaro, Pontrelli, et al., 2009). This means that the effect of the reaction at the contact line is equivalent to the resistance due to the presence of a second non-wetting component as dense and viscous as the wetting one (Sergi et al., 2014). This approach does not explain the origin of the linear behavior for the infiltration kinetics generally ascribed to effects of the reactivity (Israel et al., 2010; Voytovych et al., 2008).

The differential equation describing capillary infiltration for two fluids with the same density ρ and dynamic viscosity μ into a single channel in 2D reads (Chibbaro, Biferale, Diotallevi, et al., 2009)

$$\frac{d^2 z(t)}{dt^2} + \frac{3\mu}{r^2 \rho} \frac{dz(t)}{dt} = \frac{\gamma \cos \theta}{r \rho L}. \quad (1)$$

The first term on the left-hand side accounts for inertial forces while the second one introduces viscous forces. The term on the right-hand side is due to capillary forces. z designates the position of the invading front, r is the radius of the channel and L its length. When inertial forces are neglected, for a shrinking radius as $r(t) = r_0 - kt$ (r_0 is the initial radius and k is the reaction-rate constant) a solution to the above equation is given by

$$z(t) = \frac{\gamma \cos \theta}{6\mu k L} [r_0^2 - (r_0 - kt)^2] + z_0. \quad (2)$$

z_0 is the initial position. For completeness, in the absence of reaction, a solution to Eq. 1 taking into account also inertial forces is obtained by (Chibbaro, Biferale, Diotallevi, et al., 2009)

$$z(t) = \frac{V_{\text{cap}} r \cos \theta}{3L} t_d [\exp(-t/t_d) + t/t_d - 1] + z_0, \quad (3)$$

where $V_{\text{cap}} = \gamma/\mu$ and $t_d = \rho r^2/3\mu$. For more general porous systems, the radius of the channel is replaced with the effective radius. Relevant studies for reactive infiltration based on dynamics can be found in Asthana, Singh, and Sobczak (2005), Gern and Kochendörfer (1997), Martins, Olson, and Edwards (1988), Messner and Chiang (1990), Sangsuwan, Orejas, Gatica, Tewari, and Singh (2001), Yang and Ilegbusi (2000).

The simulations output is in model units. For the units of the basic quantities of mass, length and time we use the symbols μ , l_u and t_s , respectively. The data obtained from simulations can be expressed in regular units of the SI system after suitable transformations (Chibbaro, Biferale, Binder, et al., 2009; Chibbaro, Costa, et al., 2009; Gross, Varnik, Raabe, & Steinbach, 2010; Joshi & Sun, 2010; Komnik, Harting, & Herrmann, 2004). For comparisons with experimental data we apply the approach based on dimensionless numbers like the Reynolds or capillary numbers (Landau & Lifshitz, 2008). For example, these numbers compare the relative strength between the effects of inertial, viscous and capillary forces. Two

Type	Diameter	Volume (10^{-3})	Filling
bimodal1	0.2/0.16	4.2/2.1	0.46
bimodal2	0.2/0.12	4.2/0.9	0.46
bimodal3	0.2/0.08	4.2/0.3	0.46
multimodal	0.2/0.16/0.12/0.08	4.2/2.1/0.9/0.3	0.46
granular1	0.2	4.2	0.46
granular2	0.16	2.1	0.46
fine1	0.12	0.9	0.46
fine2	0.08	0.3	0.44

Table I: Relevant data for the packing structures composed of spheres. Multiple values for their average size are given in the case of bimodal and multimodal mixtures. Figure 1 visualizes some examples in 2D.

systems are assumed to be equivalent when the dimensionless numbers for the dominating forces have the same values. For our purposes, we also need dimensionless numbers involving the characteristic time set by the surface reaction (Sergi, Camarano, Molina, Ortona, & Narciso, 2016):

$$Q_1 = \frac{\rho r v k}{\gamma}, \quad Q_2 = \frac{\rho r k}{\mu}, \quad Q_3 = \frac{k}{v}.$$

v indicates a characteristic velocity for the system. Q_1 compares the reaction with surface tension, Q_2 the reaction with viscosity, Q_3 the reaction with inertia. For completeness, $Q_4 = \rho r v^2 / \gamma$ compares inertia with capillary forces. In our terminology, the first force becomes more important as the dimensionless number increases. In our notation, the Reynolds and capillary numbers are given by $Re = \rho v r / \mu$ and $Ca = v \mu / \gamma$. In the onset of pore closure, Q_1 tends toward zero faster and thus surface tension is the dominant force. Instead, inertia has the weakest effects since Q_3 diverges while Q_1 and Q_2 tend to 0. By using for the time-varying effective radius the average value $r_0/2$, we arrive at the same conclusions.

For the characterization of the porous systems we use Darcy law (Sukop & Thorne, 2010):

$$v \phi = -\frac{K}{\mu} \nabla P.$$

v is the interstitial velocity, ϕ the porosity, P the pressure and K the permeability. Another quantity that we take into account is the tortuosity (Bear, 1972). It is defined as the ratio of the actual length of the capillary paths to the corresponding length of the sample. For the computations we use the formula $\langle u \rangle / \langle u_x \rangle$ (Duda, Koza, & Matyka, 2011; Matyka & Koza, 2012), where u is the magnitude of the fluid velocity of components u_x and u_y . It is worth recalling that at the interface there are spurious currents (Wagner, 2003).

3. PACKING SYSTEMS

It is standard practice to reproduce the microstructure of composite materials with random packings (Scocchi et al.,

Type	Side	Volume (10^{-3})	Filling
bimodal1	0.2/0.16	9/3.9	0.44/0.45/0.38
bimodal2	0.2/0.13	9/1.9	0.45/0.46/0.40
bimodal3	0.2/0.08	9/0.6	0.44/0.46/0.45
multimodal	0.2/0.16/0.13/0.08	9/3.9/1.9/0.6	0.47/0.44/0.45
granular1	0.2	9	0.44/0.43/0.34
granular2	0.16	3.9	0.43/0.44/0.33
fine1	0.13	1.9	0.41/0.42/0.33
fine2	0.08	0.6	0.39/0.38/0.34

Table II: Basic information for the porous systems obtained from the packing of rhombs. The height of the rhombs is comparable to the length of their four equal sides, i.e. $h = 0.2, 0.16, 0.12, 0.08$. Bimodal and multimodal mixtures are characterized by multiple data for the size of the particles. The values for the filling fraction correspond to different orientations of the particles: aligned, misaligned, misaligned and tilted, respectively. Examples for the porous structures in 2D are shown in Fig. 1.

2013; Torquato, 2002). The problem consists in filling the empty space with particles arranged in a disordered way. The realization of high volume fractions can also be quite challenging (Donev et al., 2004). The principle of the algorithm for the random sequential addition is to place one particle after the other in the simulation domain (Sherwood, 1997; Widom, 1966). In case of overlapping between a test particle and an existing one, the trial is not accepted and a new particle is considered. This procedure is iterated up to the desired filling fraction. With this algorithm it is not easy to exceed values beyond 0.6.

In order to generate the packing systems for the LB simulations we employ the algorithm proposed in the article by

Type	Side	Volume (10^{-3})	Filling
fiber1	0.28/0.2	1/9	0.39/0.40/0.41
fiber2	0.28/0.16	1/3.9	0.40/0.41/0.39
fiber3	0.28/0.13	1/1.9	0.41/0.40/0.37
fiber4	0.24/0.2	0.9/9	0.39/0.40/0.41
fiber5	0.24/0.16	0.9/3.9	0.40/0.41/0.39
fiber6	0.24/0.13	0.9/1.9	0.41/0.42/0.37
fiber7	0.2/0.2	0.7/9	0.40/0.40/0.41
fiber8	0.2/0.16	0.7/3.9	0.40/0.41/0.40
fiber9	0.2/0.13	0.7/1.9	0.41/0.41/0.37

Table III: Data for the packing structures obtained with fibers and rhombs. For the side and the volume, the first value refers to the sticks and the second to the rhombs. For fibers, the side of the square base is 0.06 long. The height of the rhombs is $h = 0.2, 0.16, 0.12, 0.08$, that is, similar to the length of the four equal sides. The reported filling fractions are associated with different orientations of the particles: aligned, misaligned, misaligned and tilted, respectively. Figure 1 shows examples of porous configurations in 2D.

Type	$z \pm \Delta z$ [lu]	$v_{\text{inf},1} (10^{-4})$ [lu/ts]	$v_{\text{inf},2} (10^{-4})$ [lu/ts]	r_{eff} [lu]	K [lu ²]	λ_1	$\lambda_2 (10^3)$	$Ca (10^{-4})$	$Q_4 (10^{-8})$	$Re (10^{-4})$
bimodal1	915 \pm 53	0.71	0.83	0.44	3.19	1.17	2.07	1.40	2.59	1.85
bimodal2	851 \pm 60	0.65	0.51	0.27	4.65	1.26	0.56	1.28	1.35	1.05
bimodal3	842 \pm 142	0.65	0.45	0.24	3.53	1.22	0.34	1.29	1.19	0.92
multimodal	852 \pm 70	0.79	0.52	0.27	2.22	1.24	0.26	1.58	2.06	1.30
granular1	814 \pm 52	1.09	0.33	0.17	2.10	1.34	0.11	2.16	2.46	1.14
granular2	838 \pm 107	0.75	0.41	0.21	1.80	1.17	0.19	1.49	1.44	0.97
fine1	790 \pm 73	0.41	0.18	0.09	1.08	1.30	0.90	0.82	0.19	0.23
fine2	827 \pm 100	0.74	0.34	0.18	0.97	1.18	0.27	1.46	1.17	0.80

Table IV: Spheres composing the packing structures infiltrated without surface growth (see Tab. I).

Type	$z \pm \Delta z$ [lu]	$v_{\text{inf},1} (10^{-4})$ [lu/ts]	$v_{\text{inf},2} (10^{-4})$ [lu/ts]	r_{eff} [lu]	K [lu ²]	λ_1	$\lambda_2 (10^3)$	$Ca (10^{-4})$	$Q_4 (10^{-8})$	$Re (10^{-4})$		
bimodal1	878 ± 65	784 ± 99	876 ± 117	0.73/0.72/1.04	0.70/0.26/0.74	0.37/0.14/0.39	5.53/0.59/4.46	1.15/1.18/1.20	0.19/0.15/0.14	1.45/1.41/2.06	2.34/0.84/5.04	1.62/0.60/2.45
bimodal2	815 ± 76	901 ± 154	849 ± 31	1.29/1.27/0.64	0.31/0.82/0.55	0.16/0.43/0.29	3.25/2.44/3.12	1.31/1.29/1.34	0.09/0.09/0.22	2.56/2.52/1.27	3.26/8.28/1.40	1.27/3.28/1.11
bimodal3	805 ± 74	835 ± 97	931 ± 151	0.73/0.79/1.08	0.26/0.44/0.95	0.14/0.23/0.50	1.01/2.13/4.59	1.24/1.20/1.21	0.27/0.15/0.20	1.45/1.56/2.14	0.87/1.70/6.96	0.60/1.09/3.26
multimodal	789 ± 75	920 ± 72	840 ± 57	0.76/0.99/0.44	0.22/0.90/0.60	0.12/0.47/0.31	1.05/6.34/3.04	1.22/1.18/1.32	0.13/0.18/2.93	1.51/1.96/0.88	0.80/5.48/0.74	0.53/2.80/0.84
granular1	813 ± 93	815 ± 105	811 ± 80	0.70/0.64/0.57	0.17/0.37/0.29	0.09/0.19/0.15	8.38/6.53/6.77	1.26/1.10/1.28	0.17/0.19/0.26	1.38/1.28/1.13	0.51/0.96/0.58	0.37/0.75/0.52
granular2	759 ± 91	835 ± 155	1014 ± 213	0.68/0.48/1.24	0.13/0.39/1.19	0.07/0.21/0.63	0.57/3.19/12.3	1.21/1.22/1.22	0.19/0.35/0.20	1.34/0.95/2.45	0.37/0.56/1.14	0.27/0.59/4.66
fine1	799 ± 100	801 ± 56	873 ± 62	0.56/0.79/0.65	0.27/0.26/0.57	0.14/0.14/0.30	1.42/2.18/10.1	1.22/1.23/1.19	0.32/0.17/0.43	1.10/1.56/1.29	0.53/1.03/1.51	0.48/0.66/1.17
fine2	799 ± 59	781 ± 99	818 ± 134	0.84/0.29/0.43	0.28/0.18/0.25	0.15/0.10/0.13	1.61/2.62/5.42	1.21/1.21/1.20	0.13/0.68/3.71	1.65/0.58/0.85	1.25/0.10/0.29	0.76/0.17/0.35

Table V: Rhombs composing the packing systems infiltrated with inert boundaries (see Tab. II). For every quantity, multiple values corresponding to different orientations of fillers: aligned, misaligned, misaligned and tilted (see Fig. 1).

Type	$z \pm \Delta z$ [lu]	$v_{\text{inf},1} (10^{-4})$ [lu/ts]	$v_{\text{inf},2} (10^{-4})$ [lu/ts]	r_{eff} [lu]	K [lu ²]	λ_1	$\lambda_2 (10^3)$	$Ca (10^{-4})$	$Q_4 (10^{-8})$	$Re (10^{-4})$		
fiber1	920 ± 224	828 ± 180	1013 ± 124	0.75/1.13/1.64	0.81/0.42/1.38	0.43/0.22/0.73	8.24/3.27/9.00	1.18/1.38/1.15	0.52/0.08/0.07	1.48/2.21/3.27	2.83/3.32/23.5	1.91/1.51/7.19
fiber2	909 ± 79	817 ± 101	973 ± 138	1.27/0.75/1.09	0.78/0.39/1.01	0.41/0.21/0.54	4.29/1.28/6.72	1.19/1.23/1.18	0.10/0.16/0.16	2.53/1.49/2.16	7.96/1.40/7.55	3.15/0.94/3.50
fiber3	945 ± 326	791 ± 125	851 ± 64	1.01/0.53/0.61	0.92/0.24/0.60	0.49/0.13/0.31	5.25/1.49/5.02	1.10/1.28/1.21	0.15/0.25/7.13	1.99/1.04/1.21	5.84/0.42/1.39	2.93/0.40/1.15
fiber4	910 ± 278	783 ± 59	846 ± 48	0.58/0.22/0.60	0.86/0.12/0.32	0.46/0.06/0.17	2.30/4.98/12.3	1.18/1.09/1.12	1.10/0.50/0.97	1.14/0.43/1.18	1.79/0.04/0.72	1.57/0.08/0.61
fiber5	851 ± 204	801 ± 91	780 ± 98	0.45/0.41/0.52	0.48/0.32/0.18	0.25/0.17/0.10	5.41/3.73/4.11	1.15/1.19/1.22	0.38/0.57/0.27	0.89/0.79/1.03	0.61/0.33/0.31	0.69/0.41/0.30
fiber6	966 ± 205	765 ± 77	823 ± 57	1.41/0.17/0.53	1.12/0.09/0.29	0.59/0.05/0.15	7.67/2.67/3.28	1.07/1.33/1.21	0.15/4.29/2.12	2.80/0.33/1.05	14.1/0.02/0.50	5.02/0.05/0.48
fiber7	834 ± 75	817 ± 78	796 ± 88	0.72/0.47/0.73	0.37/0.37/0.23	0.20/0.20/0.12	2.66/1.28/5.19	1.23/1.23/1.19	0.18/0.33/0.19	1.43/0.91/1.45	1.21/0.50/0.77	0.85/0.55/0.53
fiber8	778 ± 81	943 ± 188	850 ± 53	0.92/1.81/1.25	0.17/0.87/0.61	0.09/0.46/0.32	2.49/5.22/2.10	1.13/1.09/1.17	0.12/0.07/0.08	1.82/3.58/2.44	0.92/17.8/5.86	0.51/4.96/2.40
fiber9	810 ± 133	978 ± 160	783 ± 150	0.83/1.33/0.26	0.33/1.04/0.15	0.17/0.55/0.08	2.59/5.82/2.31	1.20/1.20/1.19	0.15/0.09/3.10	1.66/2.65/0.52	1.44/11.6/0.06	0.87/4.37/0.12

Table VI: Fibers added to the packing systems infiltrated without reactive boundaries (see Tab. III). For every quantity, multiple values refer to different orientations of fillers: aligned, misaligned, misaligned and tilted (see Fig. 1).

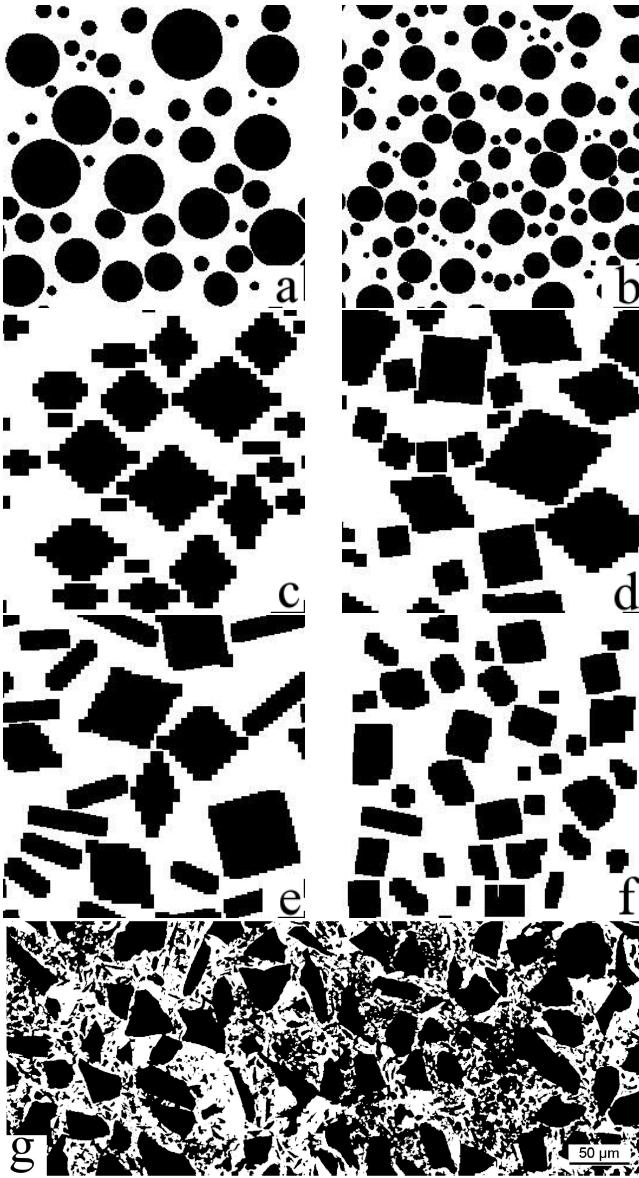


Figure 1: 2D sections for packing structures; in dark the filler particles. Information on the whole structures can be found in Tabs. I-III. (a) System bimodal1 for spheres; (b) system fine1 for spheres; (c) system multimodal for blocks; (d) system bimodal3 with misalignment for blocks; (e) system fiber1 for misalignment; (f) system fiber6 for misalignment and tilt. (g) Microstructure of a typical preform.

Sergi, D'Angelo, Scocchi, and Ortona (2012). The method consists in decomposing the particles into small cubes. The lengths are measured in units of the small cubes composing the particles according to the rule $\ell = (n+1)r$. n is the number of cubes and $2r$ their side length. Here, we consider spheres, rhombs and sticks with a certain degree of randomness for their size. For a given value of n , the associated lengths are chosen with a Gauss distribution of average ℓ and standard deviation $\sigma = \ell/4$. When the rotation of the particles is allowed, the rotation angles around the three axes are at most $\theta_x = \theta_y = \pi/2$ and $\theta_z = \pi/4$. The domain is a cube of side

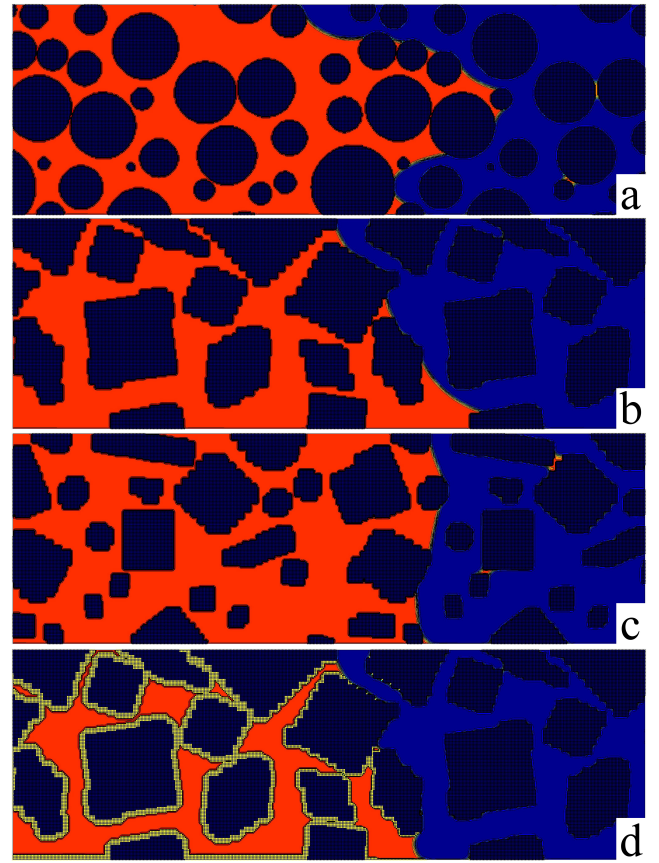


Figure 2: Fluid invasion for selected packing structures after 10^6 ts. Red is used for the wetting fluid and blue for the non-wetting component. The initial solid phase is represented in dark and the growing surface from the reaction in yellow. More details on the properties of the packing systems can be found in Tabs. I-III. More details on the results of infiltrations are reported in Tabs. IV-VII. (a) Simulation for the system bimodal1 with spherical particles. The formation of a finger can be recognized. (b) Infiltration for the system bimodal2 with rhombs in the presence of misalignment. The front will further advance because it can hit the corner of another particle before losing its curvature. (c) Visualization of the system with fibers of type fiber2 with misalignment and tilt. Tilted fibers result in the presence of small grains in 2D sections favoring infiltration as for bimodal size distributions. (d) Simulation for the system bimodal2 for rhombs with misalignment and surface reaction enabled (cf. panel b). Infiltration stops because of pore closure.

1 divided into $N = 256$ bins. The porous medium for the LB simulations is obtained by suitably replicating the packing systems. The minimal distance between two small cubes is $d_{\min} = 2/N$. An external pressure is applied toward the center of the domain in order to obtain more compact structures when necessary, as it is the case for higher degrees of disorder, for example. The other parameters for the pressure are the same as in Sergi et al. (2012).

The packing systems aim at reproducing basic characteristics resulting from the use of common commercial powders for preform preparation. In order to make the distinction between round-shaped and sharp-edged morphologies for the

Type	z_{\max} [lu]	$v_{\text{inf},1}$ (10^{-4}) [lu/ts]	r_{eff} [lu]	Q_1 (10^{-8})	Q_2 (10^{-5})	Q_3 (10^{-2})	Ca (10^{-4})	Q_4 (10^{-4})	Re (10^{-4})
bimodal1	810/781/793	0.73/0.91/1.33	0.83/0.54/0.77	0.36/0.29/0.61	2.48/1.61/2.32	6.82/5.47/3.77	1.45/1.78/2.61	5.28/5.22/16.1	3.63/2.94/6.16
bimodal2	812/839/804	1.57/1.08/0.54	0.98/1.38/0.91	0.91/0.88/0.29	2.94/4.14/2.73	3.19/4.65/9.24	3.10/2.11/1.05	28.7/18.8/3.10	9.23/8.91/2.96
bimodal3	815/810/846	1.46/1.13/1.15	1.03/1.00/1.49	0.89/0.67/1.02	3.08/3.01/4.47	3.44/4.43/4.33	2.89/2.23/2.28	25.9/15.2/23.5	8.96/6.79/10.3
multimodal	778/848/780	0.99/1.88/0.70	0.63/1.18/0.69	0.37/1.32/0.29	1.89/3.53/2.06	5.05/2.65/7.18	1.94/3.75/1.38	7.27/49.9/3.97	3.75/13.3/2.87
granular1	822/827/826	1.32/1.15/1.37	1.00/0.82/1.12	0.78/0.56/0.91	3.00/2.45/3.35	3.78/4.34/3.64	2.61/2.30/2.72	20.6/13.0/25.1	7.92/5.65/9.21
granular2	763/783/855	0.88/0.61/1.04	0.47/0.61/1.52	0.25/0.22/0.94	1.42/1.83/4.56	5.67/8.21/4.82	1.74/1.20/2.06	4.36/2.69/19.5	2.51/2.23/9.47
fine1	788/789/863	0.99/1.16/1.27	0.71/0.82/1.25	0.41/0.57/0.93	2.12/2.47/3.74	5.07/4.31/3.94	1.93/2.29/2.49	8.06/13.1/23.6	4.18/5.73/9.48
fine2	774/781/833	0.89/0.66/1.05	0.64/0.64/1.19	0.32/0.25/0.74	1.91/1.92/3.57	5.63/7.61/4.78	1.70/1.30/2.07	5.76/3.27/15.5	3.39/2.52/7.47

Table VII: Surface reaction enabled for the infiltration of packing systems obtained from rhombs (see Tabs. II and V). For every quantity, multiple values are associated with different orientations of the fillers: aligned, misaligned, misaligned and tilted (see Fig. 1).

	Q_1	Q_2	Q_3	Ca	Q_4	Re
LB systems	$2.55 \cdot 10^{-9}$	$1.45 \cdot 10^{-5}$	$2.81 \cdot 10^{-2}$	$1.76 \cdot 10^{-4}$	$9.06 \cdot 10^{-8}$	$5.16 \cdot 10^{-4}$
real systems	$1.48 \cdot 10^{-16}$	$2.71 \cdot 10^{-8}$	$0.80 \cdot 10^{-2}$	$5.47 \cdot 10^{-9}$	$1.85 \cdot 10^{-14}$	$3.39 \cdot 10^{-6}$

Table VIII: Characteristic dimensionless numbers for infiltrations in the presence of surface growth. The results for LB simulations are obtained from the systems with higher resolution leading to Fig. 7. In the case of real systems, typical experimental parameters are used (see Sec. 5.2).

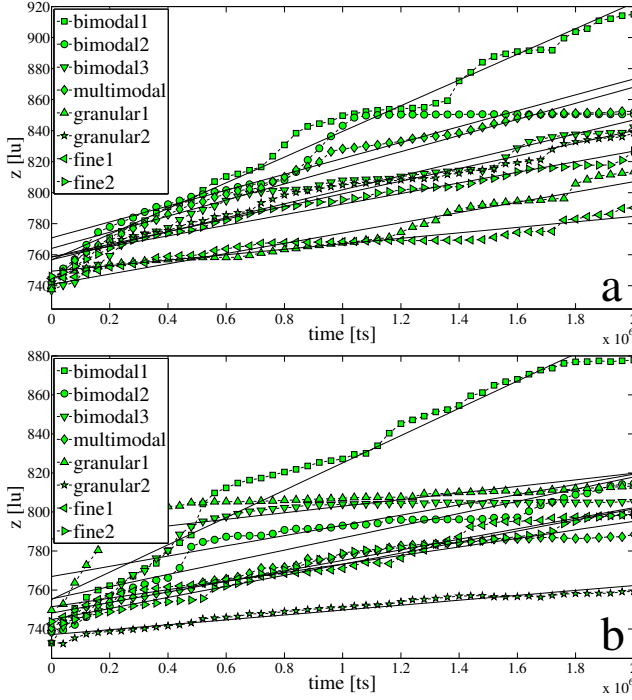


Figure 3: Infiltrated distance with chemical inertness for the solid surface. Points represent simulation results. The solid lines are fits to the data using Eq. 3. (a) Packing structures obtained from spheres; (b) packing structures realized with aligned rhombs. Basic properties of the packing systems are listed in Tabs. I and II.

particles, we consider spheres and rhombs. For example, the latter geometry can approximate the elongated shape of SiC particles. Fibers are also used as an attempt to understand the role of long walls. Concerning the size, the distribution is bimodal, multimodal or monomodal (coarse and fine particles). The properties of the packing systems are summarized in Tabs. I-III. Figure 1 shows the section for some systems.

4. SETTINGS FOR LB SIMULATIONS

As said before, the LB method is based on the discretization of the velocity space and a statistical treatment of the particle motion. In the BGK approximation for the collisions (Bhatnagar, Gross, & Krook, 1954), LB simulations remain versatile, efficient and accurate. Proper hydrodynamic behavior can be recovered in the incompressible limit at low Mach numbers (Chen & Doolen, 1998). The domain for simula-

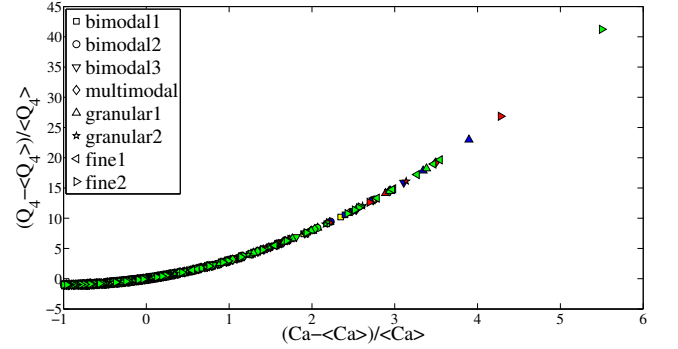


Figure 4: Relationship between the fluctuations of characteristic numbers Q_4 and Ca for packing systems with spheres and rhombs in the absence of surface reaction. Yellow markers are used for spheres, blue for aligned rhombs, red for rhombs with misalignment and green for rhombs with misalignment and tilt (see Tabs. I and II).

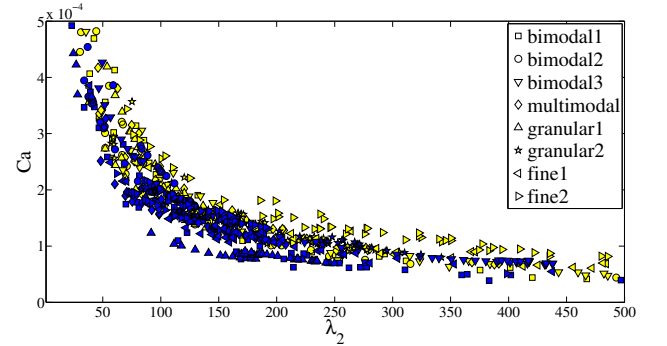


Figure 5: Relationship between the capillary number and the tortuosity as obtained from the process of capillary infiltration in the absence of reactivity. The packing structures are composed of spheres for yellow markers and of aligned rhombs for blue markers. The properties of the packing systems are summarized in Tabs. I and II.

tions is $N_x = 1500$ lu long and $N_y = 255$ lu wide. The porous structure has a length of $L = N_x/2$ and the solid-liquid interface starts at $x = 2N_x/5$. The total number of timesteps is given by $N_t = 2 \cdot 10^6$ ts. In the region occupied by the porous structure the boundaries of the simulation domain are solid and subject to the common bounce-back rule; elsewhere they are periodic. This is done in order to reduce the phenomenon of pinning near narrow-to-wide parts (Blow, Kusumaatmaja, & Yeomans, 2009; Chibbaro, Biferale, Binder, et al., 2009; Chibbaro, Costa, et al., 2009; Kusumaatmaja, Pooley, Girardo, Pisignano, & Yeomans, 2008; Moggetti & Yeomans,

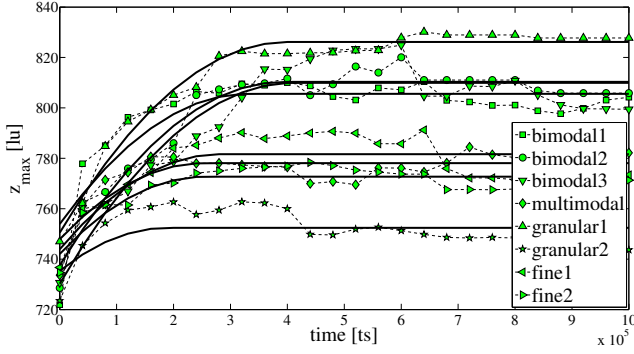


Figure 6: Average maximum of the invading front as time goes on for infiltrations with surface reaction. The porous structures are obtained from the packing of rhombs with aligned particles (see Tab. II). Points represent simulation results. The solid lines are fits to the data by means of Eq. 2.

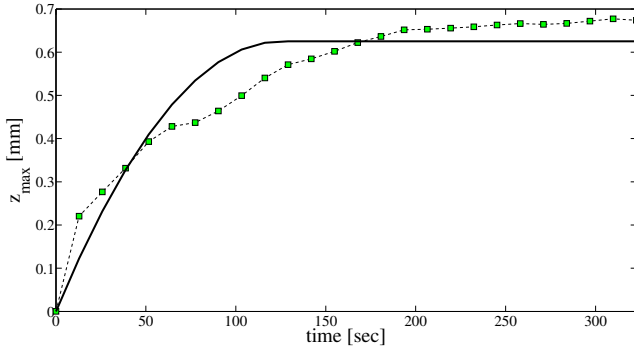


Figure 7: LB simulations for experimental results with surface growth. Average maximum for the infiltrated length as a function of time. Points are used for results from simulations. The solid line is a fit to the data with Eq. 2.

2009; Wiklund & Uesaka, 2012, 2013). The reason is that pinning can result in a significant slowdown of infiltration or even stop the flow. As explained before, the problem is studied with a two-component system, or binary mixture (Chibbaro, 2008; Chibbaro, Biferale, Diotallevi, et al., 2009; Sukop & Thorne, 2010). The viscosity is kept fixed with a relaxation time of $\tau = 1$ ts for both components. This choice is in general a guarantee for numerical stability (Sukop & Thorne, 2010). In the initial condition, half of the simulation domain is filled with the wetting fluid and the remaining with the non-wetting one. At start, the density for the main component is $\rho = 1.95$ mu/lu² and that for the dissolved component $\rho = 0.05$ mu/lu². The parameter for fluid-fluid interactions (cohesive forces) is set to $G_c = 0.9$ lu/mu/ts² (Martys & Chen, 1996; Sukop & Thorne, 2010), resulting in a surface tension of $\gamma = 0.16403$ lu·mu/ts² (Sergi et al., 2014). Solid-fluid interactions (adhesive forces) are determined by the parameters $G_{ads,1} = -G_{ads,2} = -0.35$ lu/ts² (Martys & Chen, 1996; Sukop & Thorne, 2010). With this choice the equilibrium contact angle turns out to be $\theta = 30^\circ$ (Sergi et al., 2014). This value is typical for Si droplets on SiC (Bougiouri et al., 2006; Voytovych et al., 2008). The details of the LB models

can be found in Sergi et al. (2014).

The process of surface growth from the reaction is introduced by relying on a purely heuristic treatment. A description based on solute transport as in Sergi et al. (2014, 2015) exhibits limitations related to the interface for solute transport. Namely, inside the porous structures the interface can form, leading to the diffusion of solute in the whole system. Therefore, in this work the reaction is implemented by making grow the surface of the solid phase behind the contact line at regular intervals of time. Precisely, the first layer around the solid boundaries is converted to solid phase after every $N_t/10$ timesteps. The reaction-rate constant is thus given by $k = 5 \cdot 10^{-6}$ lu/ts. This framework has the advantage to be suitable for a critical volume of simulations allowing to observe effects of pore structure and surface growth on fluid flow. Unless stated otherwise, these settings are maintained in the sequel.

5. RESULTS AND DISCUSSION

5.1 Packing systems

In Tab. IV we report the results of simulations for systems obtained from the packing of spheres in the absence of surface reaction. Here z indicates the penetration attained on average at the end of the process. Δz is an estimate of the deviations from the average. This quantity is determined from the maximum and the minimum of the front displacement. It is to be noted that the error Δz is comparable to the infiltrated distance. This means that the fluid advances into the porous medium through selected pathways (see Fig. 2). It can be expected that these fingers then contribute to fill the pores left behind. It is worth noticing that the average error is 82 lu while the size of the largest particles is on average of 51 lu. In Fig. 3 is shown the kinetics of invasion. It turns out that the infiltration is slower for a monomodal distribution of the particle size. By fitting the data with Eq. 3, we derive the infiltration velocity $v_{inf,2}$ and the effective radius r_{eff} (see Tab. IV). It can be seen that the effective radius is one to two orders of magnitude smaller than the average particle size, as stressed in previous works (Einset, 1996; Patro, Bhattacharyya, & Jayram, 2007). The permeability K is determined under the conditions usually employed to reproduce Poiseuille flow, i.e. with a single fluid, periodic boundaries and an external acceleration (Sukop & Thorne, 2010). In Tab. IV it can be seen that the permeability for spheres is higher with bimodal size distributions. In order to assess the role of interface dynamics, the tortuosity is computed in two different ways. λ_1 is determined in the presence of an external acceleration as for the permeability. λ_2 is instead obtained from the process of infiltration driven by capillary forces. The results of Tab. IV show that λ_2 is two orders of magnitude higher. As a consequence, the interface dynamics induced by the pore structure plays a prominent role. $v_{inf,1}$ is obtained by an average over the velocities inside the porous media in the direction of infiltration, i.e. x . The difference with $v_{inf,2}$ is more marked when the process is slower. For a proper basis of comparison with systems in-

cluding the reaction, the characteristic dimensionless numbers are calculated by means of $v_{\text{inf},1}$ (see Tab. IV). It is also interesting to consider the Mach number defined as $Ma = v/c_s$, where $c_s = \sqrt{1/3}$ lu/ts is the speed of sound. From Tab. IV it can be seen that the order of magnitude of Ma is 10^{-4} . It follows that in this study the numerical error associated with the LB scheme remains in the tolerance limits (He & Luo, 1997; Sukop & Thorne, 2010).

The results of simulations without reactivity for packings of particles with the shape of rhombs are reported in Tab. V. Figure 3 shows the kinetics in the case of aligned rhombs. Comparison with the outcome for packings of spheres indicates that the structure arising from rhombs is more subject to pinning. It turns out that, as the degree of disorder increases, the infiltration becomes faster. The fastest infiltrations are obtained with tilt and misalignment, even though the tortuosity λ_2 attains a larger value on average. The dynamics with spheres remain still faster or at least comparable. A possible explanation for this observation is that the arrangement of rhombs can give rise to channels that are filled easily. The shortcoming is that the phenomenon of pinning becomes more frequent. In 3D in a real preform, we expect that the advantages should prevail since the connectivity of the pore chambers is higher and the number of pathways increases. For example, the particle walls above or below a 2D section and almost parallel to it contribute to reduce pinning. This point will become clearer from the discussion on the advantages of bimodal size distributions. As expected, the permeability K is higher with increasing orientation disorder (see Tab. V). For aligned systems it also turns out that K attains higher values in the presence of larger particles. Figure 4 shows the range of variation of Ca . The same behavior holds for Re : the same relation between Re and Ca is of course an identity. More marked variations are observed for Q_4 . The increase can amount to one order of magnitude. It is interesting to note that the deviations from the average values are stronger for rhombs since the filling of distinct channels and depinning introduce more accelerations. From the order of magnitude of the average values of Ca , Q_4 and Re , we conclude that the effects of inertia are weak and capillary forces remain the dominant ones. Furthermore, in Fig. 5 it can be seen that for a given capillary number, the tortuosity seems to be slightly lower for aligned rhombs in a comparison with spheres. This tendency is recognized also in the presence of orientation disorder and for fluctuations of Ca . For clarity, this suggests that, when the fluid accelerates, the tortuosity is not higher and thus the resistance of inertia has a weak effect. So, in this case the averages of dimensionless numbers still provide an exhaustive description. As expected, it follows that the interface dynamics induced by the pore structure seems to play a more important role for the pronounced difference between λ_1 and λ_2 . Spurious currents at the interface should average out since we could verify that, when the fits allowing to obtain $v_{\text{inf},2}$ are more precise, the discrepancies with $v_{\text{inf},1}$ are smaller. Again, for aligned rhombs, it arises that liquid penetration tends to be better with a bimodal distribution. This trend is less clear with misalignment and tilt. It should be said that, in this case, 2D sections loose to a large extent the specific characteristics

of the particles composing the packings. For this reason, it might be presumed that, in 3D, bimodal distributions should remain more advantageous. Examination of the data associated with the maxima and minima for infiltration reveals that pinning is the discriminating factor coming into play. The basic mechanism at the origin of pinning is that the meniscus advances slowly while loosing its curvature, resulting in a drop of capillary pressure. In the presence of channel walls, the front can travel a longer distance since the pinning sites are not vertically aligned. As a consequence, the meniscus can encounter the surface of new particles with higher probability before halting (see Fig. 2). In the packings with small particles the pinning sites are instead generally separated by small distances. The probability that the invading front stops moving is thus higher. It is also interesting to note that rhombs with bimodal distributions pack more efficiently. On average the filling fraction of their 2D sections is 14% higher than in the case of monomodal distributions. However, their infiltrations remain faster on average of 3%. It can be seen that the results are more sensitive to specific porous configurations than to the porosity. For more clarity, test simulations are performed for different porosities for the three bimodal systems composed of rhombs with particles aligned and misaligned. For filling fractions of 36% – 50% the penetration depth varies within a narrow range on average. This is partly in line with our discussion for the conditions helping the advancement of fluid. The porosity seems to start becoming detrimental for a filling fraction approaching 60%.

Packing structures with sticks are also considered in order to make clearer the role of channels arising from the arrangement of particles introducing long walls. Table VI summarizes the results of simulations. It is manifest that the systems with alignment lead to the fastest infiltrations. Furthermore, within this group the dynamics tend to be faster in the presence of longer sticks. These results show that fibers favor the formation of preferential infiltration paths. This comes out also from the high values of the error Δz on the average penetration depth. With orientation disorder, results of rhombs and fibers are still comparable (cf. Tab. V). Sticks introduce more channels that are filled easily, inducing stronger accelerations. This appears also from the fluctuations of Ca and Re that turn out to be more marked, displaying also higher peaks (results not shown for brevity). Nevertheless, also for this set of data, capillary forces remain the dominant ones. It is interesting to note that the simulations with misalignment and tilt can lead to quite fast infiltrations, even though the number of channels is lower. A possible explanation is that orientation disorder for fibers can be regarded as equivalent to the presence of small particles when 2D cross-sections are considered (see Fig. 2). As a consequence, when the meniscus slides along the walls introduced by fibers, it is likely to encounter the surface of other particles before the interface becomes flat and pinning occurs. So, the results for fibers confirm the advantages identified for pore configurations associated with bimodal size distributions. The permeabilities for packings with fibers are more informative on the performance of the porous systems for capillary infiltration than in the presence of rhombs. It is also interesting to consider the influence of the surface area

of the solid phase (Bear, 1972), i.e. the length of its boundary for 2D structures. In principle, for a given volume, spherical shapes tend to minimize the surface area while thin oblate spheroids maximize it. It is found that for systems obtained from spheres and rhombs, the boundary length of the solid phase is higher for the systems composed of small particles, in particular for spheres. The boundary of the solid phase is longer in the case of aligned fibers. With orientation disorder, the length of the solid boundary is still longer than that of systems with rhombs. By considering for the solid phase its surface area divided by its volume, known as specific surface (Bear, 1972), it is found that the systems with fibers exhibits higher values than bimodal systems on average. The specific surface is in use for the characterization of powders. For our systems, the specific surface is lower for rhombs because it is easier to realize compact packings with coarse particles. The highest values are obtained with fibers that have however the advantage to favor the formation of channels.

Simulations in the presence of surface growth are performed for packing structures composed of rhombs (see Tabs. II and V). A typical configuration is shown in Fig. 2. Figure 6 shows examples of infiltration kinetics. At the interface between the solid and the wetting fluid the front retreats as the surface grows. This effect is more important when agglomerates of particles merge. In the analysis of the data, we thus consider an average over the highest values for the position of the front. Fits to Eq. 2 allow to obtain the initial effective radius r_0 . The effective radius used in order to determine the characteristic numbers is set to the average value: $r_{\text{eff}} = r_0/2$. The question arises whether infiltrations stop because of pore closure or pinning. Examination of the fastest dynamics indicates that the cause due to pore closure is as frequent as that for the barrier introduced by pinning. This implies that surface growth enhances the phenomenon of pinning. Indeed, it is found that in the period considered for the fits, the infiltrations without surface reaction are on average 5.7% faster. The resistance of surface growth is more marked for the fastest dynamics, i.e. with higher orientation disorder. At the point where infiltration stops according to the theoretical model of Eq. 2, the results with surface growth are comparable to that with inert boundaries. But it is to be noted that r_0 turns out to be underestimated in particular for the longer infiltrations where the front can overcome pinning barriers. More details for the results are summarized in Tab. VII. It can be seen that orientation disorder is associated with faster infiltrations. Bimodal size distributions lead to better results for aligned and misaligned particles. This is no more true with the addition of tilt. In any case, it can be expected that, in 3D porous structures, bimodal size distributions still present more advantages. In Tab. VII, the infiltration velocities are higher than in Tab. V. With surface reaction, the dynamics is shorter and the initial fast infiltration has more weight. It should be kept in mind that now the dominant effect is the infiltration interruption directly caused or induced by surface growth. With surface growth allowed, Ca , Q_4 and Re increase appreciably (see Tab. V). Furthermore, their fluctuations are by a factor of 2 smaller than for inert boundaries. Q_4 gains on average one order of magnitude, but the effects of capillary and vis-

cous forces remain more significant. This arises also from the characteristic numbers involving the properties of surface reaction Q_1 , Q_2 and Q_3 . These quantities describe better the systems because infiltration stops under the action of surface growth. Q_1 is more accurate because the effects of capillary forces are second in importance even though their relevance weakens with respect to viscosity and inertia in the presence of surface growth. Only the fluctuations of Q_3 in a few cases can deviate from the average value more than one order of magnitude.

5.2 Comparison with experiments

We now want to carry out simulations for typical experimental results with pure Si (Eustathopoulos, 2015; Israel et al., 2010). The initial porosity of the preform can be assumed to be 0.3 with initial average pore diameter of $d = 10 \mu\text{m}$. The pore size distribution is assumed to be quite narrow, with pores mainly in the range $7 - 13 \mu\text{m}$ (diameters). The preform is composed of graphite particles with average size of $70 \mu\text{m}$. The reaction-rate constant is $k = 4 \cdot 10^{-8} \text{ m/s}$ (Messner & Chiang, 1990). The other parameters of Si are $\rho = 2.53 \cdot 10^3 \text{ kg/m}^3$ for the density, $\mu = 0.94 \cdot 10^{-3} \text{ N}\cdot\text{s/m}^2$ for the viscosity and $\gamma = 0.86 \text{ N/m}$ for the surface tension (Einset, 1996). For the infiltration velocity we use $v = 5 \mu\text{m/s}$ (Eustathopoulos, 2015). Thus, the holding time for the experiment can be estimated to be $t_{\text{pc}} = 125 \text{ sec}$. From the average pore radius it follows that at this time, indicated by t_{pc} , pore closure occurs and the infiltration stops. The maximal infiltration depth results to be $z_{\text{max}} = 0.625 \text{ mm}$. The effective radius is estimated using Dullien model as in the article by Einset (1996). By taking into account the thickening of the surface of $2.5 \mu\text{m}$ leading to the average pore diameter $d/2$, it is found that an estimate for the effective radius is $r_{\text{eff}} = 0.25 \mu\text{m}$. Indicatively, in industrial practice targeted by us (e.g., manufacturing of burners and radiation plates), the C preforms are obtained starting from powders with bimodal size distributions. The size of the largest particles can vary in the range of $30 - 70 \mu\text{m}$. The size of the smallest particles can be assumed to be $5 \mu\text{m}$. For example, typical experimental work would proceed as described in the articles by Israel et al. (2010) and Voytovych et al. (2008).

Given the above experimental conditions, for the simulations we consider systems $N_x = 1500 \text{ lu}$ long and $N_y = 511 \text{ lu}$ wide. Since the width is twice longer than before, roughly speaking the infiltration velocity may double, as suggested by Eqs. 2 and 3. The length of the samples is again $L = N_x/2$, placed in the simulation domain as described in Sec. 4. The total number of timesteps is now set to $N_t = 4 \cdot 10^6 \text{ ts}$. The surface grows after every $N_t/10$ timesteps. In simulations, the reaction-rate constant is thus given by $k = 2.5 \cdot 10^{-6} \text{ lu/ts}$. All the other parameters for the LB simulations remain unchanged. The porous structures are obtained from the packing of rhombs with average side and height corresponding to 36 lu and 31 lu . Both misalignment and tilt are allowed. The resolution of the systems does not allow to include small particles as in industrial applications. The porosity of the resulting sys-

tem is 0.64. In this case, the sides of the unit cube defining the porous structure are subdivided into 512 bins. Simulations are performed for 30 sections in 2D. The correspondence with experimental results is established by imposing the experimental values for z_{\max} and t_{pc} .

Figure 7 shows the kinetics of infiltration as obtained from simulations. As done before, an average is taken over the highest values for the positions of the fronts. It can be seen that the model predicts a more abrupt behavior for the interruption of penetration, as observed also in experiments (Israel et al., 2010). It turns out that after an initial fast dynamics, the infiltration velocity decreases and in the last stage the maximal depth is attained slowly. For the sake of clarity, we consider suitable averages in the neighborhood of the point where pore closure occurs and in the ensuing interval of time where a plateau is expected to form. It is found that for 63% of the systems the infiltrated distance increases more than 10% after the time t_{pc} where pore closure is predicted by the model for the data of Fig. 7. On average, the further advancement amounts to 45%. For the remaining 37% of the systems after the time t_{pc} the fronts travel on average an additional distance corresponding to 0.6%. It is verified that in this case the flow interruption can be ascribed to pinning. As a result, the value of t_{pc} determined by the model is practically associated with the first pinning barrier. When the plateau start forming the effect of surface growth seems to remain mainly indirect. It is to be noted that the simulations reveal the tendency that the interruption of invasion is affected by the combination of the effects of surface growth, tortuosity and interface dynamics. In principle, it is reasonable to presume that the infiltration may stop before the time required for the obstruction of the average radius since the process of infiltration is described by an effective radius. However, we find that in the simulations the effect of pinning is more critical than expected in experiments. In order to elucidate the role of the effective radius more experiments are also needed for given well-known reaction-rate constants (Israel et al., 2010).

In Tab. VIII the characteristic numbers of simulations and experiments are compared. The objective is to assess the quality of the equivalence between experimental and simulation conditions. It appears that the effects of capillary forces are too weak with respect to the effects of surface growth and viscous forces. For the capillary number it is well known that high values satisfy $Ca > 10^{-2}$. For this reason, it could be questioned if the difference for the orders of magnitude of Q_1 is of particular relevance. For sure, our approach allows to establish an equivalence for the dynamics of the average penetration depth. Instead, the details of the invasion process can not be taken for granted. For example, for estimates based on the average radius of the porous structure, in experiments, when the infiltration stops because of pore closure, the ratio of the infiltrated distance to the thickness of the reaction-formed SiC is 125. In simulations, it is obtained 75. As discussed above, the relation between the average and effective radii deserve attention but a major hurdle in order to achieve better results is represented by the phenomenon of pinning. These simulations also prove that a higher resolution is not sufficient in order to reduce pinning. Again, we see that the structure is

more important than the average radius, of course increasing with a higher resolution. Under the conditions of these simulations, the average size of the particles is $150 \mu\text{m}$ while the target was $70 \mu\text{m}$ for an equivalence with a stronger direct correspondence for the porous structure. It is not easy to improve the comparison because with packings composed of smaller particles, pinning would become even more important. Furthermore, if we use the data associated with the first point in Fig. 7 exceeding the average of z_{\max} over the last 10 frames taken into account for the fit, the improvement is relative. The reason is that the velocity decreases but the initial effective radius r_0 increases. The result is that Q_1 and Ca remain of the same order. Thus, it is not straightforward in the simulations to reduce the velocity, to keep r_0 small and to weaken the phenomenon of pinning at the same time.

6. CONCLUSIONS

In this work, LB simulations are proposed for the study of capillary infiltration into porous structures. Optimization principles for the manufacturing of ceramic materials through reactive melt infiltration are at the center of our attention. In this aim, first are considered porous systems realized with the packing of particles with different properties (shape, size distribution, orientation disorder). Without surface growth, our analysis shows that the invading front tend to select preferential pathways. This can result in the formation of fingers. The data also indicate that bimodal size distributions display better infiltrations than monomodal distributions. The improvement is found to be 4.1% on average (see Tabs. IV and V). Pinning of the contact line appears as the primary factor affecting liquid penetration. Structural disorder can reduce its effect. Interestingly, bimodal size distributions present advantages in order to limit pinning. Larger faceted particles introduce walls giving rise to channels. As a result, the meniscus travels longer distances before the loss of its curvature. The probability to encounter the surface of other particles is even higher with the addition of smaller particles. The results for packings with fibers support this view. It is also verified that inertia effects induced by transient accelerations remain of secondary importance. Surface growth results in a clear interruption of the flow. This can occur because pinning turns out to be enhanced or for the pore-closing phenomenon. The retardation effects are more marked for the fast dynamics with a higher degree of orientation disorder. Again, the results point out that bimodal size distributions appear to be able of accommodating optimal infiltration. Simulations with higher resolution are also performed for a comparison with experiments. The relative strength of capillary forces turns out not to be strong enough. As a result, the infiltration dynamics is not reproduced in full details. Furthermore, the effects of surface growth for the interruption of infiltration are basically indirect in this case. We identify two aspects significant for further advances. First, the relation for the interruption of infiltration with the physical (e.g., average and minimum) and effective radii needs to be elucidated. Second, longer infiltrated lengths should be realized in simulations. A major obstacle to im-

provements resides in the over-occurrence of pinning. This situation could be improved by considering other combinations of surface tension, viscosity and, especially, contact angle (Chibbaro, Costa, et al., 2009). This could also be an extension of this work to Si alloys. Finally, our study develops a simulation work relevant for increasing the quality of ceramics obtained from LSI. Despite a poor statistics and noisy results, operational guidelines are highlighted. Further research is necessary in order to sharpen the conditions determining the optimal configuration for the porosity. Experimental tests would also allow to understand the robustness of our findings based on simplified systems.

Acknowledgments

The research leading to these results has received funding from the European Union Seventh Framework Programme (FP7/2007-2013) under grant agreement n° 280464, project "High-frequency ELectro-Magnetic technologies for advanced processing of ceramic matrix composites and graphite expansion" (HELM).

-
- [1] Aghajanian, M., Emmons, C., Rummel, S., Barber, P., Robb, C., & Hibbard, D. (2013). Effect of grain size on microstructure, properties and surface roughness of reaction bonded SiC ceramics. In J.L. Robichaud, M. Krödel, W.A. Goodman (Eds.), *Proceedings of SPIE: Vol. 8837. Material Technologies and Applications to Optics, Structures, Components and Sub-Systems* (pp. 88370-88378). Bellingham, Washington: SPIE Press. doi:10.1117/12.2024308
 - [2] Alava, M., Dube, M., & Rost, M. (2004). Imbibition in disordered media. *Advances in Physics*, 53, 83-175. doi:10.1080/00018730410001687363
 - [3] Alawadhi, E.M. (2010). *Finite element simulations using ANSYS*. Boca Raton, Florida: Taylor & Francis.
 - [4] Asthana, R., Singh, M., & Sobczak, N. (2005). Infiltration processing of ceramic-metal composites: The role of wettability, reaction, and capillary flow. *Journal of the Korean Ceramic Society*, 42, 703-717.
 - [5] Bao, N., Yibo, S., Jiao, K., Yin, Y., Du, Q., & Chen, J. (2014). Effect of gas diffusion layer deformation on liquid water transport in proton exchange membrane fuel cell. *Engineering Applications of Computational Fluid Mechanics*, 8, 26-43. doi:10.1080/19942060.2014.11015495
 - [6] Bear, J. (1972). *Dynamics of fluids in porous media*. New York, New York: Elsevier.
 - [7] Benzi, R., Succi, S., & Vergassola, M. (1992). The lattice Boltzmann equation: Theory and applications. *Physics Reports*, 222, 145-197. doi:10.1016/0370-1573(92)90090-M
 - [8] Bhatnagar, P., Gross, E., & Krook, A. (1954). A model for collision processes in gases. I. Small amplitudes processes in charged and neutral one-component systems. *Physical Review*, 94, 511-525. doi:10.1103/PhysRev.94.511
 - [9] Blow, M.L., Kusumaatmaja, H., & Yeomans, J.M. (2009). Imbibition through an array of triangular posts. *Journal of Physics: Condensed Matter*, 21, 464125. doi:10.1088/0953-8984/21/46/464125
 - [10] Bohn, R.B., & Garboczi, E.J. (2003). User manual for finite element and finite difference programs: A parallel version of NISTIR-6269 (NIST Internal Report No. 6997). Gaithersburg, Maryland: Building and Fire Research Laboratory, National Institute of Standards and Technology.
 - [11] Bougiouri, V., Voytovych, R., Rojo-Calderon, N., Narciso, J., & Eustathopoulos, N. (2006). The role of the chemical reaction in the infiltration of porous carbon by NiSi alloys. *Scripta Materialia*, 54, 1875-1878. doi:10.1016/j.scriptamat.2006.02.015
 - [12] Chen, S., & Doolen, G.D. (1998). Lattice Boltzmann method for fluid flows. *Annual Review of Fluid Mechanics*, 30, 329-364. doi:10.1146/annurev.fluid.30.1.329
 - [13] Chibbaro, S. (2008). Capillary filling with pseudo-potential binary Lattice-Boltzmann model. *The European Physical Journal E*, 27, 99-106. doi:10.1140/epje/i2008-10369-4
 - [14] Chibbaro, S., Biferale, L., Binder, K., Dimitrov, D., Diotallevi, F., Milchev, A., & Succi, S. (2009). Hydrokinetic simulations of nanoscopic precursor films in rough channels. *Journal of Statistical Mechanics: Theory and Experiments*, 6007-6021. doi:10.1088/1742-5468/2009/06/P06007
 - [15] Chibbaro, S., Biferale, L., Diotallevi, F., & Succi, S. (2009). Capillary filling for multicomponent fluid using the pseudo-potential Lattice Boltzmann method. *The European Physical Journal Special Topics*, 171, 223-228. doi:10.1140/epjst/e2009-01032-8
 - [16] Chibbaro, S., Costa, E., Dimitrov, D.I., Diotallevi, F., Milchev, A., Palmieri, D., ... Succi, S. (2009). Capillary filling in microchannels with wall corrugations: A comparative study of the Concus-Finn criterion by continuum, kinetic, and atomistic approaches. *Langmuir*, 25, 12653-12660. doi:10.1021/la901993r
 - [17] Dezellus, O., & Eustathopoulos, N. (2010). Fundamental issues of reactive wetting by liquid metals. *Journal of Materials Science*, 45, 4256-4264. doi:10.1007/s10853-009-4128-x
 - [18] Dezellus, O., Hodaj, F., & Eustathopoulos, N. (2003). Progress in modelling of chemical-reaction limited wetting. *Journal of the European Ceramic Society*, 23, 2797-2803. doi:10.1016/S0955-2219(03)00291-7
 - [19] Diotallevi, F., Biferale, L., Chibbaro, S., Lamura, A., Pontrelli, G., Sbragaglia, M., ... Toschi, T. (2009). Capillary filling using lattice Boltzmann equations: The case of multi-phase flows. *The European Physical Journal Special Topics*, 166, 111-116. doi:10.1140/epjst/e2009-00889-7
 - [20] Diotallevi, F., Biferale, L., Chibbaro, S., Pontrelli, G., Toschi, F., & Succi, S. (2009). Lattice Boltzmann simulations of capillary filling: Finite vapour density effects. *The European Physical Journal Special Topics*, 171, 237-243. doi:10.1140/epjst/e2009-01034-6
 - [21] Donev, A., Cisse, I., Sachs, D., Variano, E.A., Stillinger, F.H., Connelly, R., ... Chaikin, P.M. (2004). Improving the density of jammed disordered packings using ellipsoids. *Science*, 303, 990-993. doi:10.1126/science.1093010
 - [22] Duda, A., Koza, Z., & Matyka, M. (2011). Hydraulic tortuosity in arbitrary porous media flow. *Physical Review E*, 84, 36319-36326. doi:10.1103/PhysRevE.84.036319
 - [23] Dullien, F.A.L. (1992). *Porous media: Fluid transport and pore structure*. San Diego, California: Academic Press.
 - [24] Einset, E.O. (1996). Capillary infiltration rates into porous

- media with application to silcomp processing. *Journal of the American Ceramic Society*, 79, 333-338. doi:10.1111/j.1151-2916.1996.tb08125.x
- [25] Einset, E.O. (1998). Analysis of reactive melt infiltration in the processing of ceramics and ceramic composites. *Chemical Engineering Science*, 53, 1027-1039. doi:10.1016/S0009-2509(97)00379-5
- [26] Eustathopoulos, N. (2015). Wetting by liquid metals-Application in materials processing: The contribution of the Grenoble Group. *metals*, 5, 350-370. doi:10.3390/met5010350
- [27] Eustathopoulos, N., Nicholas, M.G., & Drevet, B. (1999). *Wettability at high temperatures*. Oxford: Pergamon.
- [28] Fan, S., Zhang, L., Xu, Y., Cheng, L., Tian, G., Ke, S., ... Liu, H. (2008). Microstructure and tribological properties of advanced carbon/silicon carbide aircraft brake materials. *Composites Science and Technology*, 68, 3002-3009. doi:10.1016/j.compscitech.2008.06.013
- [29] Furler, P., Scheffe, J., Gorbar, M., Moes, L., Vogt, U., & Steinfeld, A. (2012). Solar thermochemical CO₂ splitting utilizing a reticulated porous ceria redox system. *Energy and Fuels*, 26, 7051-7059. doi:10.1021/ef3013757
- [30] Gadow, R. (2000). Current status and future prospects of CMC brake components and their manufacturing technologies. In T. Jessen & E. Ustundag (Eds.), *Proceedings of the 24th Annual Conference on Composites, Advanced Ceramics, Materials, and Structures A: Vol. 21* (pp. 15-29). Hoboken, New Jersey: Wiley & Sons. doi:10.1002/9780470294628.ch2
- [31] Gadow, R., & Speicher, M. (2000). Optimized morphological design for silicon infiltrated microporous carbon preforms. In T. Jessen & E. Ustundag (Eds.), *Proceedings of the 24th Annual Conference on Composites, Advanced Ceramics, Materials, and Structures A: Vol. 21* (pp. 485-492). Hoboken, New Jersey: Wiley & Sons. doi:10.1002/9780470294628.ch57
- [32] de Gennes, P.G., Brochard-Wyart, F., & Quéré, D. (2004). *Capillarity and wetting phenomena: Drops, bubbles, pearls, waves*. New York, New York: Springer.
- [33] Gern, F.H., & Kochendörfer, R. (1997). Liquid silicon infiltration: Description of infiltration dynamics and silicon carbide formation. *Composites Part A: Applied Science and Manufacturing*, 28, 355-364. doi:10.1016/S1359-835X(96)00135-2
- [34] Ghosh, S., Patil, P., Mishra, S.C., Das, A.K., & Das, P.K. (2012). 3-D lattice Boltzmann model for asymmetric Taylor bubble and Taylor drop in inclined channel. *Engineering Applications of Computational Fluid Mechanics*, 6, 383-394. doi:10.1080/19942060.2012.11015429
- [35] Goodall, R., & Mortensen, A. (2014). Porous metals. In D.E. Laughlin & K. Hono (Eds.), *Physical Metallurgy* (pp. 2399-2595). Waltham, Massachusetts: Elsevier. doi:10.1016/B978-0-444-53770-6.00024-1
- [36] Gross, M., Varnik, F., Raabe, D., & Steinbach, I. (2010). Small droplets on superhydrophobic substrates. *Physical Review E*, 81, 51606-51619. doi:10.1103/PhysRevE.81.051606
- [37] Haghani, R., Rahimian, M.H., & Taghilou, M. (2013). LBM simulation of a droplet dripping down a hole. *Engineering Applications of Computational Fluid Mechanics*, 7, 461-470. doi:10.1080/19942060.2013.11015485
- [38] He, X., & Luo, L.S. (1997). Lattice Boltzmann model for the incompressible Navier-Stokes Equation. *Journal of Statistical Physics*, 88, 927-944. doi:10.1023/B:JOSS.0000015179.12689.e4
- [39] Hillig, W.B., Mehan, R.L., Morelock, C.R., DeCarlo, V.J., & Laskow, W. (1975). Silicon/silicon carbide composites. *American Ceramic Society Bulletin*, 54, 1054-1056.
- [40] Israel, R., Voytovych, R., Protsenko, P., Drevet, B., Camel, D., & Eustathopoulos, N. (2010). Capillary interaction between molten silicon and porous graphite. *Journal of Materials Science*, 45, 2210-2217. doi:10.1007/s10853-009-3889-6
- [41] Joshi, A.S., & Sun, Y. (2010). Wetting dynamics and particle deposition for an evaporating colloidal drop: A lattice Boltzmann study. *Physical Review E*, 82, 41401-41417. doi:10.1103/PhysRevE.82.041401
- [42] Komnik, A., Harting, J., & Herrmann, H.J. (2004). Transport phenomena and structuring in shear flow of suspensions near solid walls. *Journal of Statistical Mechanics: Theory and Experiment*, 2004, 12003. doi:10.1088/1742-5468/2004/12/P12003
- [43] Koponen, A., Kandhai, D., Hellén, E., Alava, M., Hoekstra, A., Kataja, M., ... Timonen, J. (1998). Permeability of three-dimensional random fiber webs. *Physical Review Letters*, 80, 716-719. doi:10.1103/PhysRevLett.80.716
- [44] Krenkel, W., & Berndt, F. (2005). C/C-SiC composites for space applications and advanced friction systems. *Materials Science and Engineering A*, 412, 177-181. doi.org/10.1016/j.msea.2005.08.204
- [45] Kusumaatmaja, H., Pooley, C.M., Girardo, S., Pisignano, D., & Yeomans, J.M. (2008). Capillary filling in pattern channels. *Physical Review E*, 77, 67301-67304. doi:10.1103/PhysRevE.77.067301
- [46] Landau, L.D., & Lifshitz, E.M. (2008). *Fluid mechanics*. Burlington, Massachusetts: Elsevier.
- [47] Liu, G.W., Muolo, M.L., Valenza, F., & Passerone, A. (2010). Survey on wetting of SiC by molten metals. *Ceramics International*, 36, 1177-1188. doi:10.1016/j.ceramint.2010.01.001
- [48] Liu, H., Valocchi, A.J., & Kang, Q. (2012). Three-dimensional lattice Boltzmann model for immiscible two-phase flow simulations. *Physical Review E*, 85, 46309-46322. doi:10.1103/PhysRevE.85.046309
- [49] Martins, G.P., Olson, D.L., & Edwards, G.R. (1988). Modeling of infiltration kinetics for liquid metal processing of composites. *Metallurgical Transactions B*, 19, 95-101. doi:10.1007/BF02666495
- [50] Martys, N.W., & Chen, H.D. (1996). Simulation of multi-component fluids in complex three-dimensional geometries by lattice Boltzmann method. *Physical Review E*, 53, 743-750. doi:10.1103/PhysRevE.53.743
- [51] Matyka, M., & Koza, Z. (2012). How to calculate tortuosity easily? In K. Vafai (Ed.), *American Institute of Physics Conference Proceedings: Vol. 1453. Porous media and its applications in science, engineering, and industry* (pp. 17-22). Melville, New York: American Institute of Physics Publishing. doi:10.1063/1.4711147
- [52] Messner, R.P., & Chiang, Y.M. (1990). Liquid-phase reaction-bonding of silicon carbide using alloyed silicon-molybdenum melts. *Journal of the American Ceramic Society*, 73, 1193-1200. doi:10.1111/j.1151-2916.1990.tb05179.x
- [53] Mognetti, B.M., & Yeomans, J.M. (2009). Capillary filling in microchannels patterned by posts. *Physical Review E*, 80, 56309-56316. doi:10.1103/PhysRevE.80.056309
- [54] Mortensen, A., Drevet, B., & Eustathopoulos, N. (1997). Kinetics of diffusion-limited spreading of sessile drops in reactive wetting. *Scripta Materialia*, 36, 645-651. doi:10.1016/S1359-6462(96)00431-9
- [55] Paik, U., Park, H.C., Choi, S.C., Ha, C.G., Kim, J.W., & Jung, Y.G. (2002). Effect of particle dispersion on microstructure and strength of reaction-bonded silicon carbide. *Materials Science and Engineering: A*, 334, 267-274. doi:10.1016/S0921-5093(01)01897-4
- [56] Patro, D., Bhattacharyya, S., & Jayram, V. (2007). Flow kinet-

- ics in porous ceramics: Understanding with non-uniform capillary models. *Journal of the American Ceramic Society*, 90, 3040-3046. doi:10.1111/j.1551-2916.2007.01776.x
- [57] Roberson, C., & Hazell, P.J. (2003). Resistance of silicon carbide to penetration by a tungsten carbide cored projectile. In E. Medvedovsk (Ed.), *Proceedings of the 105th Annual Meeting of the American Ceramic Society: Vol. 151. Ceramic armor and armor systems* (pp. 165-174). Hoboken, New Jersey: Wiley & Sons. doi:10.1002/9781118406793.ch14
- [58] Salamone, S., Karandikar, P., Marshall, A., Marchant, D.D., & Sennett, M. (2008). Effects of Si:SiC ratio and SiC grain size on properties for RBSC. In E. Lara-Curzio, J. Salem, D. Zhu (Eds.), *Ceramic Engineering and Science Proceedings: Vol. 28. Mechanical properties and performance of engineering ceramics and composites III* (pp. 101-109). Hoboken, New Jersey: Wiley & Sons. doi:10.1002/9780470339497.ch10
- [59] Sangsuwan, P., Orejas, J.A., Gatica, J.E., Tewari, S.N., & Singh, M. (2001). Reaction-bonded silicon carbide by reactive infiltration. *Industrial & Engineering Chemistry Research*, 40, 5191-5198. doi:10.1021/ie001029e
- [60] Scocchi, G., Ortona, A., Grossi, L., Bianchi, G., D'Angelo, C., Leidi, T., & Gilardi, R. (2013). Evaluation of a simple finite element method for the calculation of effective electrical conductivity of compression moulded polymer-graphite composites. *Composites: Part A*, 48, 15-25. doi:10.1016/j.compositesa.2012.12.013
- [61] Sergi, D., D'Angelo, C., Scocchi, G., & Ortona, A. (2012). Random packing of small blocks: Pressure effects, orientational correlations and application to polymer-based composites. *Particle & Particle Systems Characterization*, 29, 24-34. doi:10.1103/PhysRevE.84.061602
- [62] Sergi, D., Camarano, A., Molina, J.M., Ortona, A., & Narciso, J. (2016). Surface growth for molten silicon infiltration into carbon millimeter-sized channels: Lattice-Boltzmann simulations, experiments and models. *International Journal of Modern Physics C*, 27, 1-24. doi:10.1142/S0129183116500625
- [63] Sergi, D., Grossi, L., Leidi, T., & Ortona, A. (2014). Surface growth effects on reactive capillary-driven flow: Lattice Boltzmann investigation. *Engineering Applications of Computational Fluid Mechanics*, 8, 549-561. doi:10.1080/19942060.2014.11083306
- [64] Sergi, D., Grossi, L., Leidi, T., & Ortona, A. (2015). Lattice Boltzmann simulations on the role of channel structure for reactive capillary infiltration. *Engineering Applications of Computational Fluid Mechanics*, 9, 301-323. doi:10.1080/19942060.2015.1026432
- [65] Sherwood, J.D. (1997). Packing of spheroids in three-dimensional space by random sequential addition. *Journal of Physics A: Mathematical and General*, 30, 839-843. doi:10.1088/0305-4470/30/24/004
- [66] Succi, S. (2009). *The lattice Boltzmann equation for fluid dynamics and beyond*. Oxford: Oxford University Press.
- [67] Sukop, M.C., & Thorne Jr, D.T. (2010). *Lattice Boltzmann modeling: An introduction for geoscientists and engineers*. Berlin Heidelberg: Springer.
- [68] Torquato, S. (2002). *Random heterogeneous materials: Microstructures and macroscopic properties*. New York, New York: Springer.
- [69] Voytovych, R., Bougiouri, V., Calderon, N.R., Narciso, J., & Eustathopoulos, N. (2008). Reactive infiltration of porous graphite by NiSi alloys. *Acta Materialia*, 56, 2237-2246. doi:10.1016/j.actamat.2008.01.011
- [70] Wang, M., & Pan, N. (2008). Modeling and prediction of the effective thermal conductivity of random open-cell porous foams. *International Journal of Heat and Mass Transfer*, 51, 1325-1331. doi:10.1016/j.ijheatmasstransfer.2007.11.031
- [71] Washburn, E.W. (1921). The dynamics of capillary rise. *Physical Review*, 27, 273-283. doi:10.1103/PhysRev.17.273
- [72] Wagner, A.J. (2003). The origin of spurious velocities in lattice Boltzmann. *International Journal of Modern Physics B*, 17, 193-196. doi:10.1142/S0217979203017448
- [73] Widom, B. (1966). Random sequential addition of hard spheres to a volume. *The Journal of Chemical Physics*, 44, 3888-3894. doi:10.1063/1.1726548
- [74] Wiklund, H., & Uesaka, T. (2012). Edge-wicking: Microfluidics of two-dimensional liquid penetration into porous structures. *Nordic Pulp and Paper Research Journal*, 27, 403-408. doi:10.3183/NPPRJ-2012-27-02-p403-408
- [75] Wiklund, H.S., & Uesaka, T. (2013). Microfluidics of imbibition in random porous media. *Physical Review E*, 87, 23006-23014. doi:10.1103/PhysRevE.87.023006
- [76] Wolf-Gladrow, D.A. (2005). *Lattice-gas cellular automata and lattice Boltzmann models - An introduction*. Berlin Heidelberg: Springer.
- [77] Yang, J., & Ilegbusi, O.J. (2000). Kinetics of silicon-metal alloy infiltration into porous carbon. *Composites Part A: Applied Science and Manufacturing*, 31, 617-625. doi:10.1016/S1359-835X(99)00089-5